This is the accepted manuscript of the article, which has been published in *Advances in Oto-rhino-laryngology*. 2019, 82, 12-31. https://doi.org/10.1159/000490268

Imaging of temporal bones.

Pyykkö I[1], Zou J[1,2], Gürkov R[3], Naganawa S[4], Nakashima T[5,6,7]

[1]Hearing and Balance Research Unit, University of Tampere, Lääkärinkatu 1, Room E222, 33520 Tampere ,Finland.

[2]Department of Otolaryngology-Head and Neck Surgery, Changhai Hospital, Second Military Medical University, Changhai Road 168, Shanghai 200433. China E-mail: Jing.Zou@staff.uta.fi

[3]Department of Otorhinolaryngology. Campus Grosshadern. University of Munich, Germany, University of Munich, Marchioninistr. 15 81377 München Germany

[4]Department of Radiology, Nagoya University Graduate School of Medicine, Nagoya, Japan, 65 Tsurumai-cho, Shouwa-ku, Nagoya, 466-8550 Japan E-mail naganawa@med.nagoya-u.ac.jp

[5] Ichinomiya Medical Treatment & Habilitation Center, 1679-2, Tomida-nagaresuji, Ichinomiya City, 494-0018, Japan

[6] Department of Otorhinolaryngology, National Center for Geriatrics and Gerontology, 7-430, Morioka-cho, Obu City, 474-8511, Japan.

[7] Department of Otorhinolaryngology, Nagoya University Graduate School of Medicine, Nagoya, Japan, 65 Tsurumai-cho, Shouwa-ku, Nagoya, 466-8550 Japan E-mail tsutomun@med. nagoya-u.ac.jp

Key words: Ear imaging, Multidetector computed tomography, cone-beam tomography, MRI, micro CT, targeted contrast agents.

Address of the corresponding author:

Ilmari Pyykkö

Itäinen Puistotie 12 A 1

00140 Helsinki, Finland

e-mail: ilmari.pyykko@uta.fi

tel: +358 40 5294314

The work has been performed at the University of Tampere, Lääkärinkatu 1, 33520 Tampere

Abstract: (200 words)

Multidetector computed tomography (MDCT) has been the benchmark for visualizing bony changes of the ear but has recently been challenged by cone-beam computed tomography (CBCT). In both methods with 2D or 3D imaging all inner ear bony structures can be visualized satisfactorily. Both of these imaging methods produce ionizing radiation and induce adverse health effects, especially among children. In 3T magnetic resonance imaging (MRI) the soft tissue can be highly accurately imaged. Use of gadolinium chelate (GdC) as a contrast agent allows the partition of fluid spaces to be visualized, such as the bulging of basilar and Reissner's membranes.. Both intravenous and intratympanic administration of GdC has been used. The development of the positive endolymph imaging method, which visualizes endolymph as a bright signal and the use of image subtraction seems to allow more easily interpretable images. This long-awaited possibility of diagnosing endolymphatic hydrops in living human subjects has enabled the definition of Hydropic Ear Disease, encompassing typical Meniere's disease as well as its monosymptomatic variants and secondary conditions of endolymphatic hydrops. The next challenge in imaging of the temporal bone is to perform imaging at the cellular and molecular level. This chapter provides an overview of current temporal bone imaging methods and a review of emerging concepts in temporal bone imaging technology.

Introduction.

Rapid development of radiological equipment over the last several decades has significantly promoted the role of imaging in otology. Computed tomography (CT) and magnetic resonance imaging (MRI) have become an integral part of the evaluation of children and adults with hearing loss and diseases associated with temporal bone. The currently used Multi Detector CT (MDCT) techniques allow bony tissue determination with an accuracy of 0.1 mm. Recently cone-beam computed tomography (CBCT) technology has become particularly attractive for temporal bone imaging as CBCT imaging reduces the exposure to ionizing radiation when compared with traditional MDCT. However, changes in inner ear fluid spaces became possible only with 3T or higher MRI equipment in combination with contrast agents and special imaging techniques.

Abnormalities on CT or MRI are found in 20% to 50% of children with sensorineural hearing loss and correlate with the degree of hearing loss(1). Imaging of the temporal bone by using both MRI and MDCT is likely the future gold standard for temporal bone imaging (2). Some recent and novel imaging methods used experimentally in temporal bones have not yet been applied clinically such as optical coherence tomography imaging (3) (4) (5), microtomography (μCT) (6) and endoscopes using coherent anti-Stokes Raman spectroscopy (CARS) technique (7) these (7), development of advanced of contrasting agents (8) and these may provide additional imaging benefits in the future. This chapter provides an overview of current temporal bone imaging methods and a review of emerging concepts in temporal bone imaging technology.

CT

CT is the most common modality for assessing the bony anatomy of the temporal bone. CT can detect signs of perilymphatic fistulae (i.e. pneumolabyrinth) but fails to detect subtle traumatic lesions within the inner ear, such as labyrinthine haemorrhage or axonal damage along central auditory pathways (9). Many anatomic structures of the middle and inner ears are not optimally depicted using conventional CT with image reconstruction in the standard axial and coronal planes. In early development of CT, cochlear partitioning and soft tissue membranes were not adequately visualized (10) (11). Recent advances in MDCT, including the development of scanners with 32 detector rows (64 effective sections) for depiction of normal anatomy and pathologic states in the temporal bone, allow the acquisition of isotropic voxels that can be reconstructed and used in the multiplanar reconstructions of volumetric CT images (12). This technique gives radiologists the opportunity to visualize the anatomic structures of the middle and inner ears accurately (table 1) (13). Recent reconstruction methods in MDCT may also allow

Legend for table 1: Synopsis of the anatomically important structures and the respective primary criteria for image quality assessment. Rated as: -= not visible, += poorly, ++= moderately and +++= good visible. (6) (54)

Structure/Condition	**Review Criteria**	**MDCT**	**CBCT**	**MRI**
Cochlea	Normal contour, 2.5 turns	+++	+++	+++
Intracochlear calcification	Ability to discern intracochlear ossifications	++	+++	+\-
Osseous spiral lamina	Presence, integrity	-	-	-
Modiolus	Presence, integrity	++	++	+
Vestibule	Contour, density	+++	+++	+
Semicircular canals	Contour, density, Hypo-/Aplasia, dehiscence	+++	+++	++
Vestibular aqueduct	Contour, density	+++	+++	+
Cochlear aqueduct	Contour, density	++	+++	+++
Cochlear nerve	Presence	+	+	+++
Bony lamella at auditory canal fundus	Presence, integrity of bony lamella separating the internal auditory canal from the cochlea	+	+	+++?
Internal auditory canal	Contour	+++	+++	+++?
Facial nerve canal, cochlear segment	Contour, course	++	+++	-
Facial nerve canal, tympanic segment	Contour, course	+++	+++	-
Facial nerve canal, mastoid segment	Contour, course	+++	+++	-
Middle ear cavity	Aeration	+++	+++	+++
Malleus	Presence of all parts	++	+++	-
Incus	Presence of all parts	++	+++	-
Stapes	Presence of all parts	++	+++	-
Round window	Presence, aperture	++	+++	-
Round window niche	Borders, aeration	++	+++	-
Oval window	Presence, borders, footplate position	++	+++	-
Internal carotid artery canal	Borders, osseous wall dehiscence	+++	+++	-
Jugular foramen / jugular bulb	Borders, osseous wall dehiscence	+++	+++	-
Mastoid	Bony borders, aeration	+++	+++	-
Perilymphatic space	Gadolinium contrasted,	-	-	+++
Endolymphatic space	Not contrasted	-	-	+++
Stria vascualris	If leaking and contrasted	-	-	+++
Cochleo-vestibular nerve	Tissue growth > 1 mm	-	-	+++
Canal for subarcuate artery	Course and contour visualized by CT and MRI	+++	?	+++
Singular canal	Course and contour visualized by CT and MRI	+++	?	+++

visualization of the cochlear partitioning (9). A recent paper by Maillot et al. (12) indicated that MDCT allows radiologists to examine the complex anatomy of the temporal bone with sub-millimeter resolution and is the first

modality of choice. Indeed, it is capable of revealing a broad spectrum of ossicular lesions that may not be apparent on the basis of clinical findings alone.

For MDCT the slice thickness is a critical point and detailed anatomical evaluation as small as 0.2 mm slice intervals have been used (12). The MDCT technique may help to overcome the limitations long imposed by restrictions in gantry angle and patient positioning and improves diagnostic accuracy. The main advantages of MDCT for temporal bone imaging are shorter acquisition times, a decrease in tube current load and better spatial resolution. The short acquisition time is an advantage especially when dealing with younger patients, or those with claustrophobia or severe pain that often need sedatives for appropriate image acquisition. The ability of MDCT to obtain images of temporal bones bilaterally in one scan is another reason why MDCT is effective for imaging the temporal bone. Additional techniques such as virtual otoscopy with 3-D reconstructions of MDCT images can provide a different view on ossicular chain anomalies in traumatic conditions (14). CT has been considered the gold-standard method for postoperative imaging of the electrode position after cochlear implantation (CI),although plain X-ray films have been used (15, 16).

In detecting a thin bony coverage of a superior semicircular canal, digital volume tomography (DVT) scans seem to be superior to MDCT scans (13). Giesemann and Hofmann (9) indicated that CT is the gold standard in imaging diagnosis of semicircular canal dehiscence syndrome (SCDS).; however, it has a high false-positive rate and may be misleading in terms of diagnosis because it overestimates the size of the dehiscence and the prevalence (17). In addition, many patients with imaging findings of superior canal dehiscence do not suffer from a clinical dehiscence syndrome. In those with SCDS there is no clear linear relationship between the size of the dehiscence and the extent of clinical symptomatology, however the dehiscence length does correlate positively with the maximal air-bone gap (17). Nevertheless, a definite diagnosis of SCDS is difficult with any radiologic imaging technique (18). It has been reported that subarcuate venous malformations cause audio-vestibular symptoms similar to those of SCDS and should be excluded in temporal bone imaging (19).

The National Cancer Institute of United States estimates that approximately 5 to 9 million CT examinations are performed annually on children all over the country (20). Despite the many benefits of CT, a disadvantage is the inevitable radiation exposure. Although CT scans comprise approximately12 per cent of diagnostic radiological procedures in large U.S. hospitals, it is estimated that they account for approximately 49 per cent of the U.S. population's collective radiation dose from all medical x-ray examinations (20). An association between increased

risk of cancer and CT scans has been reported especially in children (21), (22) (23). The National Cancer Institute of United States estimates that a radiation dose of 50 mSieverts (mSv) increases of the risk of cancer by threefold, particularly in children (20, 22, 24). This dose reflects CT imaging performed in 5-10 head CT scans. The lifetime cancer mortality risk is estimated to be approximately 14% per Sv for a 1-year-old child, 5% per Sv for a middle-aged adult, and based on current models less than 2% per Sv for an individual older than 60 years (23).

To avoid high radiation dose the novel "low dose protocols" of MDCT have been developed and a compromise between dose and resolution has been made (25) (26). The tube current-time product and voltage can be reduced by 50% without increasing artefacts. (26) Low-dose postoperative MDCT scans are sufficient for localizing the CI electrode (26) and reduce metal artefacts (25). The application of conventional CT in otolaryngology might be replaced by cone-beam computed tomography (CBCT) in the future (27, 28). For congenital malformations of the inner ear MDCT has a long history and is an outstanding tool to visualize anatomical changes. Ultra-high resolution CT (UHR-CT) with collimation of 0.25mm is coming to clinical field soon (29). Future study is warranted to compare the ability of CBCT and UHR-CT, although CBCT might have the advantage in terms of radiation dose reduction.

CBCT

In CBCT, a pulsed cone shaped X-ray beam performs a single rotation around a patient simultaneously acquiring all of the necessary volumetric data for the reconstruction of separate images in the sagittal, coronal, and axial planes. In the temporal bone any interface between two materials (as from fluid to the bone), is a step in tissue anatomy, but like a ramp in the CBCT image. The width of the ramp depends on factors such as detector pixel size, image acquisition geometry and radiation source focal spot size. This process differs from traditional MDCT that reconstructs images using a series of axial slices. CBCT creates less streak artefacts and offers higher spatial resolution than MDCT (cubic voxel size of approximately 0.07 mm versus 0.1 –0.6 mm, respectively). Erovic et al. (27) promoted the use of CBCT in intraoperative monitoring of the temporal bone. CBCT has a smaller footprint compared with MDCT, which makes it more feasible for use in outpatient departments or operating theatres. CBCT is reportedly capable of demonstrating fine structures of the middle and inner ears as well as pathological diseases within temporal bone, such as otosclerosis (30). In the assessment of SCDS, CBCT is suggested to be more reliable than MDCT (31).

CBCT appears to provide sufficient spatial accuracy for intraoperative usage during temporal bone surgery (32) (27). Identifying the location of implants is becoming increasingly important in modern otology, which involves applications such as the Vibrant Soundbridge implant and CI (6, 33) (34). With regard to monitoring the electrode array location during CI surgery, there is an emerging need to improve the imaging quality to better assess electrode trauma to the fine structures of the cochlea, such techniques include low-dose iterative reconstruction, scatter correction, lag correction, and metal artifact reduction (35) (36) (37) (38). Gupta et al. (39) refined the technology for temporal bone imaging using a smaller detector element and acquired a total of 900 cone-beam projections under a field of view of 15.5 cm; however, the image quality was not perfect. Furthermore, metal electrodes tend to cause artifacts that may blur the images (40). In assessment of the location of the cochlear implant with CBCT Pearl et al (41) could not clearly detect the basilar membrane to designate exact scalar location, which is consistent with previous reports. Zou et al (6) used the osseous spiral lamina of cochlea to assess the location of cochlear implant and to delineate between the scalae (Fig. 1). The scalar position, has also been evaluated by Ruivo et al. (42) and Verbist et al. (43), and in their study the osseous spiral lamina was visible in all sections.

Figure 1. A cochlear implant electrode located in the cochlea imaged with CBCT. Osseous spiral lamina is visible in all turns and the locations of electrodes are typically leaning on the lateral wall in the scata tympani. With permission of Acta Otolaryngol (Stokh.) (32).

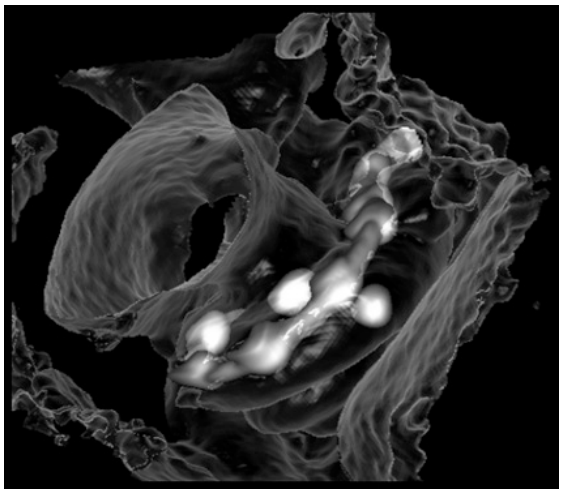

Ruivo et al (42) concluded that CBCT provides high-resolution and almost artefact-free multiplanar reconstruction images allowing assessment of the precise intracochlear position of the electrode and visualization of each of the individual contacts; the CBCT visualization consisted of 23 middle and inner ear structures using a 5-point scale.

They showed that insufficient image-quality scores were more frequent in low-dose scans versus high-dose scans, however, the difference was only statistically significant for otologists but not for neuroradiologists. Image quality was critical for small structures (such as the stapes or lamella at the internal auditory canal fundus). The CBCT images can discern individual electrode contacts, often not possible on MDCT (44) (45). In addition, Pearl et al (41) demonstrated that CBCT improved imaging of the cochlea and facial nerve canal, enabling identification of electrode contacts in close proximity to the fallopian canal and therefore most prone to induce inadvertent stimulation of the facial nerve.

Zou et al (42) (28) evaluated the effects of filters, voltage and frame numbers in visualization of the inner ear using CBCT among isolated human temporal bones; each temporal bone was independently analysed by two imaging engineers and 3 otologists; each investigator had at least 15 years of experience with temporal bone CT and were blinded to the dose-relevant scan parameters during the review of the scan. In 2D imaging in all temporal bones the land marks of modiolus, osseous spiral lamina, and bony wall of cochlear duct that isolate scala vestibuli from scala tympani were demonstrated at a level in that the anatomic structures were fully assessable in all parts and acceptable image quality (table 1). Basilar membrane was not visualized in the cochlea. Changes in the tube current from 8 mA to 12.5 mA resulted in a minimal change of the temporal bone image quality. The tube voltage of 80 kV provided best images using 900 frames. In 3D images contrasts adjustment allowed very high quality of imaging of inner ear (fig. 2). The low X-ray dose is mostly a result of the small region scanned and the low kV used in CBCT (79 kV). The reason why the artefacts in the work of Zou et al. (6) were relatively minor in comparison of a previous work is that a suitable adjustment on the "γ curve" of the original images that suppresses the metal artefacts on the images was employed, and in addition improved imaging sharpness was achieved by using a pause during each exposure (e.g., start-stop-expose-start-stop-expose) together with high frames of two dimensional images, which was not previously reported (38).

Figure 2. CBCT imaging using 900 frame numbers and 1.72 magnification factor on a temporal bone. A sharp image of the stapes was demonstrated in the temporal bone. Abbreviations: AC: anterior crus; FP: footplate; PC: posterior crus. ISJ: incudo-stapedial joint; LPI: lenticular process of incus. The black scale bar in the right lower corner = 2.5 mm. With permission of Annals of Otology, Rhinology & Laryngology (49).

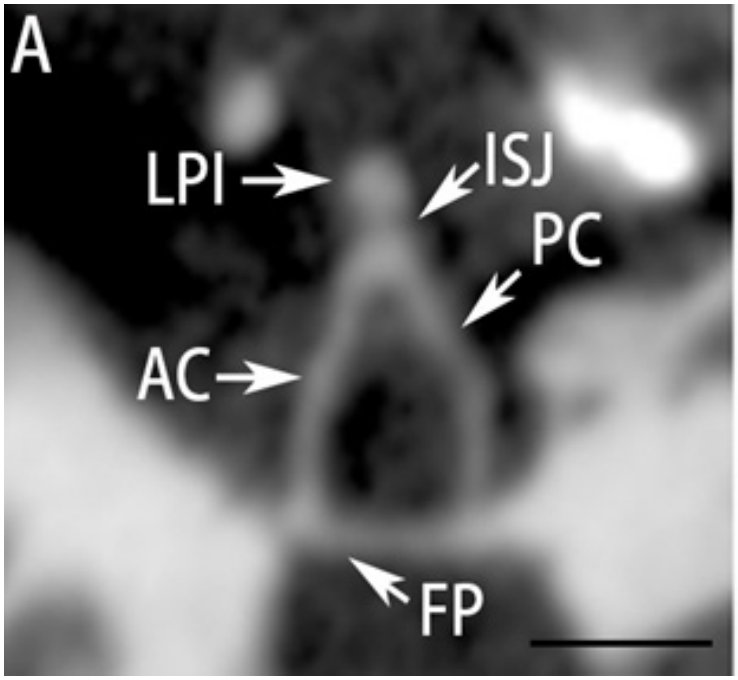

With CBCT the full course of the subarcuate canal from the subarcuate fossa to the mastoid antrum can be accurately visualized, and the accompanying air cells were distinguished from the subarcuate canal in a temporal bone with a pneumatized superior semicircular canal wall (46) (47). The novel high-resolution CBCT system potentially has the power to detect changes associated with SCCD.

A comparison of low-dose MDCT and CBCT image quality after cochlear implantation revealed that the visibility of cochlear inner and outer walls and overall image quality were positively correlated with radiation dose on MDCT; image quality was better with clinical MDCT than with CBCT protocols (48). In other comparisons, differences between systems were found, but a distinction between CBCT and MDCT could not be made (48). The effective radiation dose of the CBCT protocols was 6 to 16% of the clinical MDCT dose.

Yamane et al. (49) evaluated the diagnostic properties of 3D CBCT images among 25 patients with Meniere's disease (MD) and 13 healthy patients. They developed algorithms to determine the optimal 3D-CBCT window settings for the detection of water, muscle, calcium carbonate, and bone (48). It was suggested that 3D CBCT imaging changes in the membranous labyrinth may be useful for the objective diagnosis of MD, that dislodged saccular otoconia may have an important role in MD, and that CBCT may be useful even in inner ear membrane imaging (48).

In CBCT the total radiation dose of the work in Zou et al (46) was 13 μSv in male phantom head... The most

dominant contributor to the effective dose was bone marrow (36%-37%) followed by brain (34%-36%), remainder tissues (12%), extra-thoracic airways (7%), and oral mucosa (5%) (46). It is important to note that in this study the dose was measured with an anthropomorphic model with controlled error marginal. These results were in accordance with results of a previous study that demonstrated effective doses between 35.2 – 137.6 µSv (50). In some reports there is estimation of even lower dose of radiation in CBCT imaging (30) but the estimated values may significantly deviate from the measured values (51). In a comparable study Erovic et al. (27) reported that the radiation dose of CBCT per scan is ~10 mGy (~0.35 mSv) to a dosimetry head phantom at 100 kVp and 170 mA, and was low compared with a typical 2 to 5 mSv diagnostic head CT and as high as 4.8 mSv have been reported (42) (52).

MRI

High resolution MRI imaging has an advantage over all types of CT imaging of the temporal bone as it provides better characterization of soft tissue and fluid-filled partitions. Despite several advantages, the major limitations of this method are the lack of bony details. Even with the recently developed ultra-short echo time pulse sequence, middle ear ossicles are only partly visualized (53{Naganawa, 2016 #1182). This is due to the lack of water containing material in the dense cortical bones. Another major disadvantage of using this method in temporal bone imaging is the high cost of the examination and the sedation needed for younger patients or patients in severe pain. In addition, this method cannot be used for implant imaging or intra-operative imaging where metal objects are involved in the operations as the superconducting magnets will attract the metals and electronic devices. For patients who are allergic to certain contrast agents, another type of contrast agent that may be more costly is required.

MRI is the modality of choice when investigating the inner ear and suspecting soft tissue growth such as vestibular schwannoma, vascular malformations, endolymphatic hydrops or pathology of the cochlear aqueduct (54). Naganawa et al. (55) (56) (57) developed specific algorithms using Fluid Attenuation Inversion Recovery sequences (FLAIR) that will demonstrate minute amounts of contrast agent in the inner ear (56) (58). The use of MRI in temporal bone imaging is dependent on the area to be visualized, the patient's age, the pathology involved and its severity level. MRI is the gold standard in radiologic evaluation of soft tissue changes in the temporal bone and may serve as a complementary method when CT is used to characterize the bony structures.

MRI diagnosis of MD has been challenging until recent years (59) The first efforts to demonstrate visualization of fluid spaces in the inner ear with GdC were carried out in animal studies by using animal MRI equipment of 4.7 T scanner (60). After demonstrating the contrasting of perilymph, Zou et all (61) (62) were the first to demonstrate that in the guinea pig endolymphatic hydrops could be visualized accurately and that the changes respected the histological verification of the degree of endolymphatic hydrops. These findings were followed by Niyazov et al. (63) who showed similar results using a clinical 1.5 T machine. In humans using 1.5T MRI, the passage of GdC delivered transtympanically, was shown to accumulate in the inner ear after 12 h post injection and fully contrasted the labyrinth after 24 h post injection. However 1.5T MRI equipment was not sensitive enough to demonstrate the delicate details of the perilymph and endolymph borders (64). Figure 3 demonstrates the cochlear fluid spaces and endolymphatic hydrops (59).

The recent development of 3T MRI provides a tool for visualizing endolymphatic hydrops with GdC as the contrast agent (65) (66) (67) (fig. 3). MRI especially in Japan ,Germany and just recently in USA has become a clinically useful tool for the diagnosis of atypical cases as well as typical cases of MD. Methodological development in imaging techniques and increase of the magnetic field strength have allowed separation of bone from fluid and contrast agent, and have improved spectral resolution, signal-to-noise ratio and contrast intensity and reduced scan acquisition times (55) (56) (68). These properties are particularly helpful in the attempt to resolve details between the minute fluid filled spaces within the inner ear (approximately50 µl for endolymph and 150 µl for perilymph!).

Figure 3. Endolymph and perilymph in the inner ear. (A) normal, (B) endolymphatic hydrops. The endolymph (gray) is surrounded by the perilymph (black) except for endolymphatic duct (ED) and endolymphatic sac (ES). U: utricle, S: saccule, St: stapes, R: round window. With permission of Auris Nasus Larynx (70)

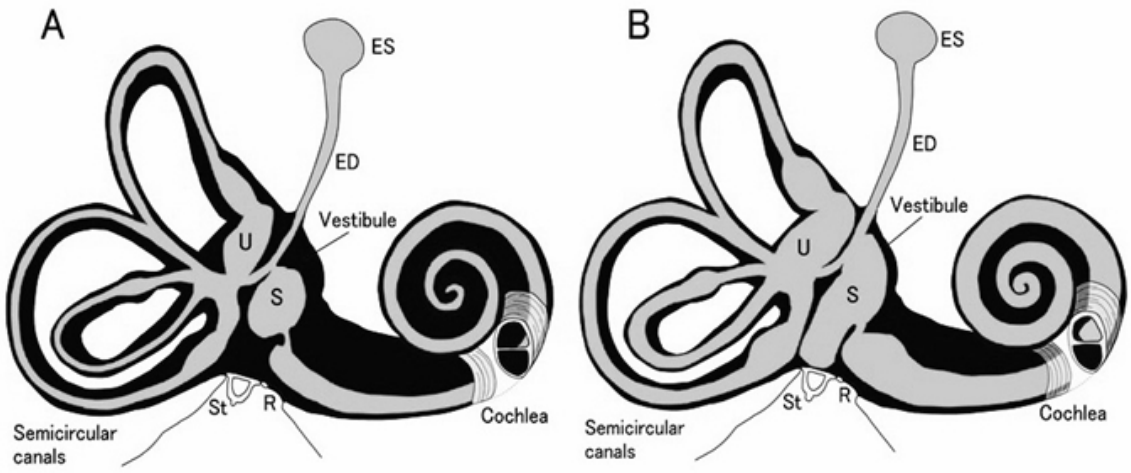

A grading scale for the degree of endolymphatic hydrops has been proposed for use in research settings that was validated using identical histologic criteria and has also been applied also to clinical evaluations (61) *(69)* (70). The normal limit of ratio of the endolymphatic area over the vestibular fluid space (sum of the endolymphatic and perilymphatic area) is 33 % and any increase in the ratio would be indicative of EH (70) (71). According to the criteria, *mild endolymphatic hydrops* in the vestibule covers the ratio of 34% to 50% and *significant endolymphatic hydrops* covers the ratio of more than 50% in the vestibule (70). The respective evaluation of the ratio of the endolymphatic area over the total fluid space in the cochlea is correlated to displacement of Reissner's membrane. Normally the Reissner's membrane remains in situ and is shown as a straight border between the endolymph containing scala media and the perilymph containing scala vestibuli. *Mild endolymphatic hydrops* displays an extrusion of the Reissner's membrane towards the scala vestibuli and results in an enlargement of the scala media with an area of less than that of the scala vestibuli. *Severe endolymphatic hydrops* causes an increase of the scala media with an area larger than that of the scala vestibule (70). A similar grading system on the ordinal level, with three degrees of severity for cochlear hydrops (mild, marked, extreme), has also been proposed (72). In cadavers without symptom history, the ratio of the endolymphatic space to the total vestibular fluid space ranged from 26.5 % to 39.4 % (70) (73)

The perilymphatic space facing the vestibule is sealed by the annular stapedial ligament and the perilymphatic space of scala tympani is sealed by the round window membrane. Animal and human experiments indicated that on

MRI the perilymphatic space in the vestibule is filled with GdC earlier and more intensively than the perilymphatic space of scala tympani (74) (75). Thus the cochlear perilymph space was often poorer filled with GdC than the vestibular part. Zou et al. performed a series of experiments by sealing either the round or oval windows and demonstrated that the permeability of the round window was poorer than that of the oval window (76) (77) (78). This explains also why treatment of severe Meniere's disease with low dose gentamicin infrequently causes deafness (less than 5% with two gentamicin injections) (79, 80) but is effective in ablation of vestibular complaints. For the visualization of inner ear membranes therefore it is important to fill the upper posterior part of the middle ear cavity with GdC so that the contrast agent has the possibility to be transported also via the oval window as the annular ligament is quite porous. Intratympanic administration of GdC provided efficient loading of the contrast agent in the inner ear perilymph and reduced the risk of systemic toxicity but raised concerns of local toxicity, as it is off label and requires puncture of the tympanic membrane. Such local toxicity was not observed during short, medium or long-term follow-up (81) (82) (83). In addition, image quality might be compromised owing to impaired GdC penetration of the round and oval window membranes (78) (84) and only the injected side of the inner ear can be evaluated (58). To evaluate both ears simultaneously, it is necessary to inject GdC into both sides (85) (68) (86). These drawbacks hinder the widespread use of this procedure (87). The development of more sensitive MRI techniques facilitates endolymphatic hydrops imaging using a single dose of intravenous GdC (56, 88) ; this method has become intensively used as clinical research method (89) (90) (91). To establish the normal range of endolymph ratio, healthy volunteers were scanned after intratympanic (70) (73) and intravenous (92) GdC applications. Figure 4 demonstrates visualization of endolymphatic hydrops with different MRI protocols.

Figure 4. Fig. 1 a 72-year-old man with the clinical suspection of left Meniere's disease. Images are obtained 4 hours after IV-SD-GBCM. Conceptual diagram for the image generation of HYDROPS-Mi2 and HYDROPS2-Mi2. Upper row images indicate the generation of HYDROPS-Mi2. HYDROPS image, which is the subtraction of positive endolymphatic image (not shown) from positive perilymphatic image (heavily T2-weighted 3D-FLAIR, not shown) is multiplied by T2-weighed MR cisternography. Note that black areas (arrows) represent endolymphatic space in labyrinth and white areas represent perilymphatic space on HYDROPS-Mi2. Contrast between endo- and perilymphatic space is very strong, while the back ground signal is quite uniform on HYDROPS-Mi2. Lower row images indicate the generation of HYDROPS2-Mi2. HYDROPS2 image, which is the subtraction T2-weighed MR cisternography from positive perilymphatic image (heavily T2-weighted 3D-FLAIR, not shown) is multiplied by T2-weighed MR cisternography. Note that black areas (arrows) represent endolymphatic space in labyrinth and white areas represent perilymphatic space on HYDROPS2-Mi2 similar to HYDROPS-Mi2. Contrast between endo- and perilymphatic space is very strong, while the back ground signal is quite uniform on HYDROPS2-Mi2 similar to HYDROPS-Mi2. With permission of Jpn J Radiol (58).

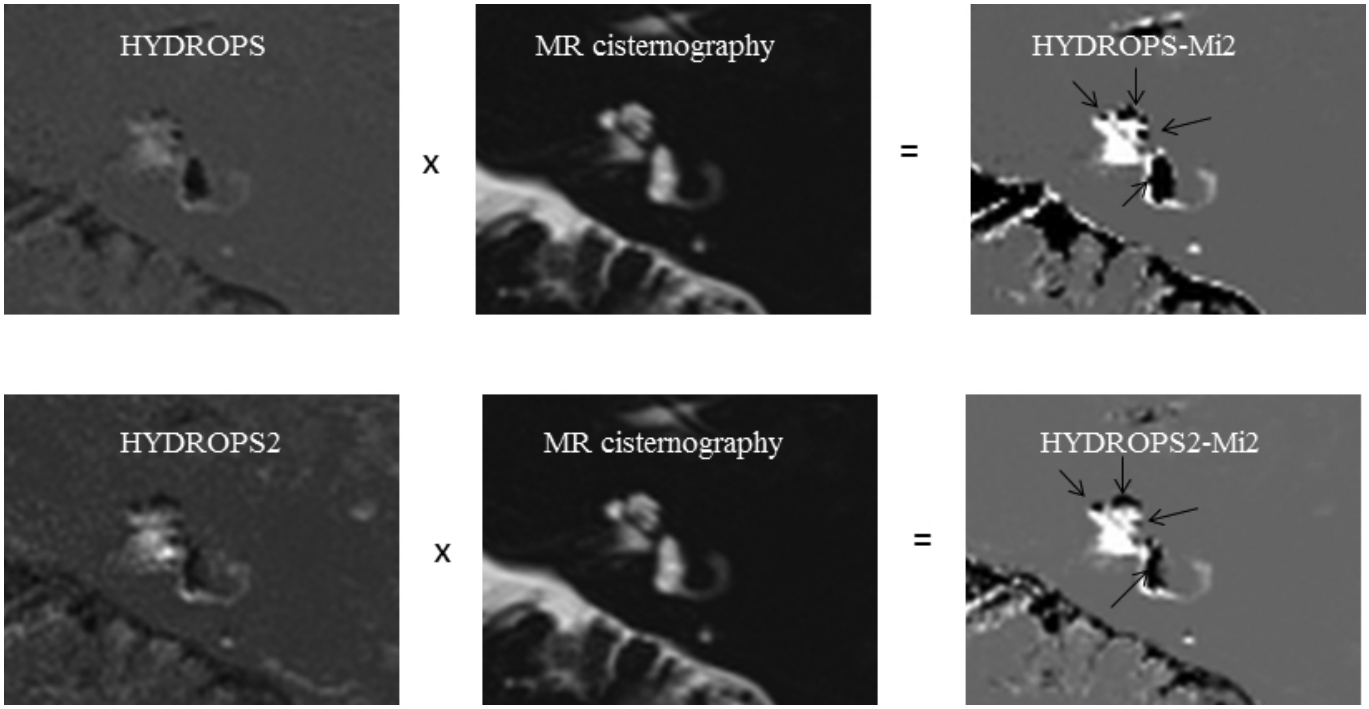

Fig. 5 A 42-years-old man with the clinical diagnosis of right sided definite Meniere's disease. Images are obtained 24 hours after IT-GdC in the right ear and 4 hours after IV-SD-GBCM. The right ear shows IT+IV-GdC effect and the left ear shows only IV-GdC effect. Note that conventional 3D-FLAIR and 3D-real IR shows the sufficient enhancement of perilymph to recognize endolymphatic space only in the IT+IV side, however heavily T2-weighted 3D-FLAIR and HYDROPS2 allows the differentiation between peri- and endolymphatic space on both IV side and IT+IV side. Significant endolymphatic hydrops (arrows) is seen in cochlea and vestibule in the right side and no endolymphatic hydrpos is seen in the left cochlea. Absence of endolymphatic hydrops in the left vestibule is confirmed in lower level slices (not shown). With permission of Jpn J Radiol. (58)

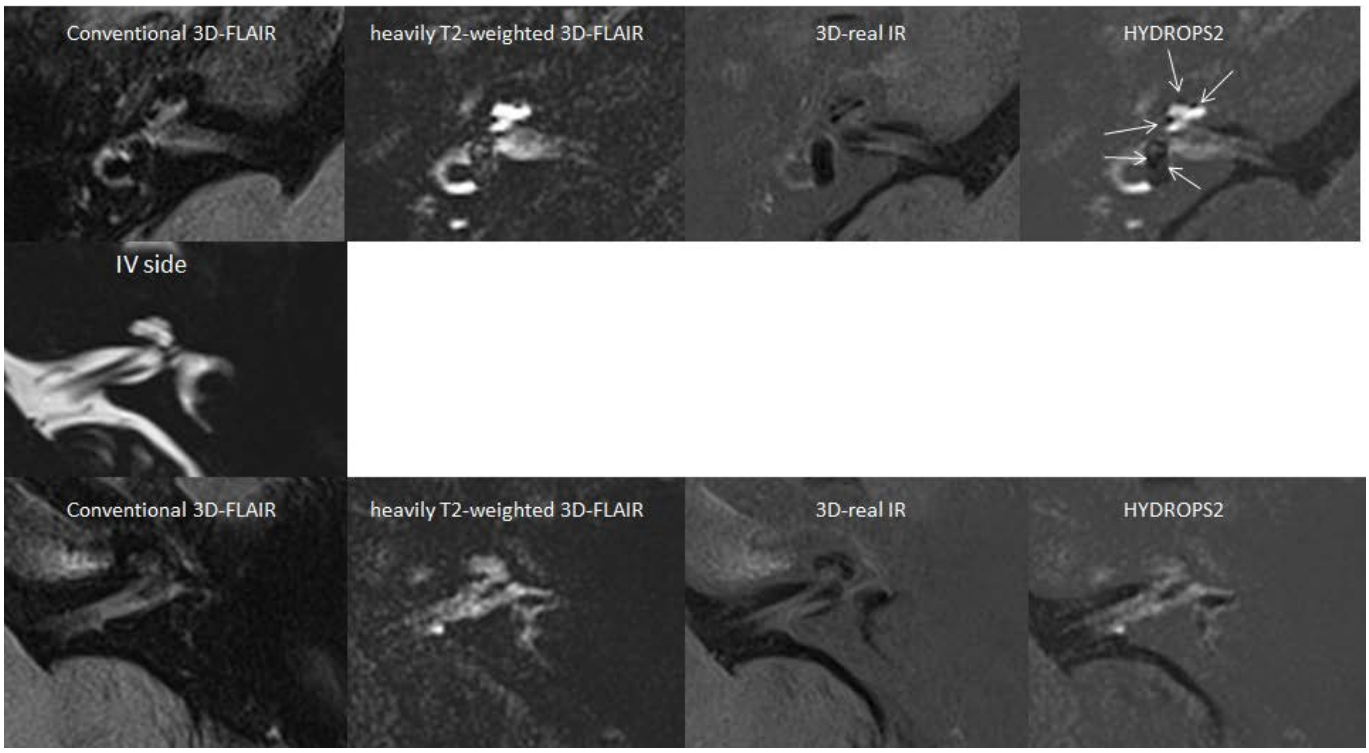

The measurement of endolymph volume ratio following 3D-real inversion recovery images obtained 24 hours after intratympanic GdC using machine learning and automated local thresholding segmentation algorithms has been reported with highly reproducible results and a highly significant correlation between hearing loss and cochlear endolymphatic hydrops (93). Semi-automated volume ratio measurement of endolymph from images obtained 4 hours after single dose intravenous GdC using short (8 minutes) and long (18 minutes) acquisition times (57) has been recommended. The correlation of the volume ratio between the long and short acquisition time images was high ranging from 0.77 (endolymphatic hydrops in the cochlea) to 0.99 (endolymphatic hydrops in the vestibule); the Pearsson's correlation coefficients were all statistical significant ($p<0.001$). Later they demonstrated that 3-Inversion-recovery turbo spin echo with real reconstruction (3D-real IR) showed higher contrast between the non-enhanced endolymph and the surrounding bone (94) (fig. 6). Regular contrast 3D-FLAIR cannot readily visualize cochlear hydrops after single dose IV-Gd, especially in apical turn. Recently Naganawa et al. developed the positive endolymph image method, which visualizes endolymph as bright signal as well as subtraction images (HYDROPS images, HYbriD of Reversed image Of Positive endolymph signal and native image of positive perilymph Signal images) and allowed more easily interpretable images (85) (95). In our experience, using heavily T2-weighted 3D-FLAIR positive perilymph image (PPI) and positive endolymph image (PEI) and subtracted images (HYDROPS technique) is useful to compensate for the lower concentration of Gd by IV. A further developed technique for generating improved HYDROPS (i-HYDROPS) images allows for a higher contrast to noise ratio per unit time compared to conventional HYDROPS imaging; this is accomplished by elongating the repetition time and increasing the refocusing flip angle(96). In the study the size of the endolymphatic space was comparable in both the i-HYDROPS and 3D-real IR images.. The 3D-real IR does not require postprocessing for subtraction and might be more robust toward slight compositional alterations in endolymph than i-HYDROPS imaging-based on magnitude reconstruction and the scan time for 3D-real IR images was 10 min.

Figure 4 (after IV. injection of GdC) and fig. 5 (after intratympanic injection of GdC) demonstrates the inner ear fluid compartments, anatomical structures and endolymphatic hydrops. Nakashima et al. (59), Pyykkö et al. (71) and Fiorino et al. (97) have demonstrated, with MRI, that endolymphatic hydrops was present in all living patients with definite MD, which is different from the reports by Shi et al. in which endolymphatic hydrops was absent in some definite MD (98). Recently it has been demonstrated that endolymphatic hydrops can affect the cochlear and

vestibular compartments differently and cause different complaints (71). However, the association between clinical symptoms and endolymphatic hydrops in individual patients is not yet clarified, as hearing can be relatively well preserved despite prominent endolymphatic hydrops (67) (99) and the extent of endolymphatic hydrops seems to vary along the course of the disease: it may increase, decrease or remain stable (100, 101) (102). With new imaging techniques, endolymphatic hydrops can be demonstrated in vivo and can confirm the diagnosis. Furthermore, it has become possible to evaluate MD using new functional tests, such as VEMP frequency tuning measurements, in patient populations with clinically and morphologically (by MRI detection of endolymphatic hydrops) confirmed diagnosis of MD (101) (103).

Figure 6.. 3D Real reconstruction inversion recovery MRI of the right ear illustrates high signal-to-noise ratio and severe cochleovestibular endolmyphatic hydrops in a patient with Meniere's disease 24 hours after intratympanic GdC application (Magnevist 1:8 diluted). Section thickness 0.3 mm. Siemens Verio scanner, 32-channel head coil. Endolymph appears black, perilymph appears white, temporal bone appears grey. The sections are positioned from left to right and from top to bottom so that they move through the inner ear in a caudal-to-cranial direction. The cochlea displays endolymphatic hydrops in all three turns. The vestibulum displays severe endolymphatic hydrops, with only a weak perilymph signal at its outer borders. The horizontal semicircular canal is completely visualized by its perilymph signal. (With kind permission of Prof. B. Ertl-Wagner, Institute of Clinical Radiology, University of Munich)

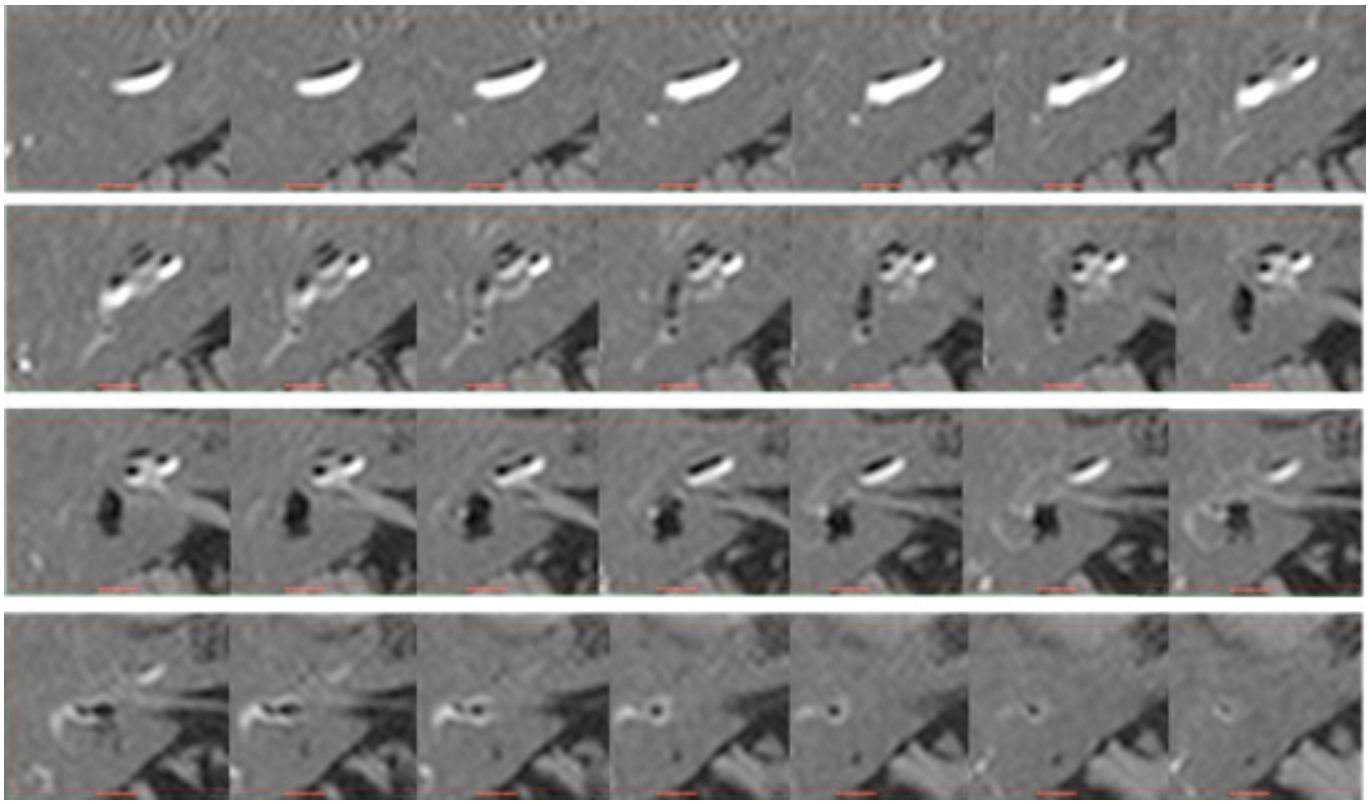

The current challenges in inner ear imaging are to improve the delivery of the contrast agent so that the concentration of GdC in the inner ear will exceed the detection limit. The transtympanic and intravenous administrations have different indications (66). If the aim is to demonstrate an endolymphatic hydrops, then transtympanic injection of GdC is preferred. Usually the transtympanic administration provides stronger uptake and is easier to assess than intravenous injection. In principle, the sensitivity of the intravenous and the transtympanic method to demonstrate endolymphatic hydrops in the inner ear should be similar based on sufficient uptake of GdC in the inner ear, as both methods measure the same phenomenon (87). A technique in which the images of inverted grey-scale positive endolymph are subtracted from images with native positive perilymph images is useful when inner ear loading of GdC is low. This subtraction significantly improves the contrast noise ratio and assists in separation of endolymph, perilymph and bone (104) or when combining intravenous injection with transtympanic injection (68).

The development of dynamic imaging techniques of the inner ear has provided several important new insights into MD; 1) the cochlear and vestibular compartments can be differently affected, and 2) in about 24 -75% of the cases the disease is bilateral (71) (105). 3) The extent of endymphatic hydrops can vary during time in individual patients (102). 4) the extent of the endolymphatic hydrops does not correlate with complaints (86). The variable latency between complaints in MD (71) and bilateral nature of the disease confirms (106) (107) the observations in MRI (71) Unilateral disease was reported to progress to bilateral disease in up to 35% of patients within 10 years and in up to 47% within 20 years of follow up (108, 109). The vestibule showed endolymphatic hydrops more frequently than did the cochlea although most commonly the endolymphatic hydrops was found in both cochlea and vestibule (71). Patients with sudden deafness and in spontaneous tinnitus often had endolymphatic hydrops (71). Whether endolymphatic hydrops will develop in all forms of tinnitus is not known but is worth studying. The application of endolymphatic hydrops imaging in patients with various inner ear symptoms and disorders has shown that endolymphatic hydrops is not only present in cases of typical MD, but also in its monosymptomatic variants and in the conditions of secondary endolymphatic hydrops. These observations have coined the term “Hydropic Ear Disease”, allowing for a logic and comprehensive classification of these disorders (110).

Furthermore, clinical imaging of endolymphatic hydrops has shown that 1) endolymphatic hydrops progresses with time, both on the cross-sectional level (72) and on the individual level (101), 2) the severity of cochlear and vestibular function deficits are generally correlated with the severity of endolymphatic hydrops (72), 3) the hydropic herniation of vestibular endolymphatic spaces into the semicircular canal can be visualized in-vivo (111) and - with the advent of accurate measurements of the vestibule-ocular reflex (VOR) at high frequencies (Video Head Impulse Test) offers a possible explanation for the well-known paradox of horizontal semicircular canal dysfunction in MD: while the (low-frequency) caloric response is impaired, the (high frequency) head impulse test is typically normal (112)(113) (114).

Legend for table 2. Inner ear pathology with MRI with different application routes of contrast agent used for visualizing different nature of the disorder.

Disease	**Membranous labyrinth injury**	**Delivery route of Gd**
Ménière's disease	Reissner's membrane bulging, rarely a rupture	Transtympanic delivery /Intravenous delivery
Inner ear immune disorder	Stria vascularis pathology/ Endolymphatic hydrops	Intravenous delivery or Intratympanic delivery
Circulatory disturbances	Stria vascularis pathology	Intravenous delivery
Spontaneous membrane rupture	Reissner's membrane	Intravenous delivery or Intratympanic delivery
Perilymphatic fistula	Round window membrane rupture or semicircular canal injury	Intravenous delivery or Intaratympanic delivery
Trauma (mechanical and noise)	Stria vascularis pathology	Intravenous delivery

In clinical practice, the question is often pending, which GdC delivery pathway should be taken; the intratympanic or the intravenous delivery? Table 2 demonstrates the alternative strategies to visualize inner ear disorders in different disease and suspected pathologies. The benefit of intratympanic delivery is that most often the GdC concentration is greater in transtympanic delivery than in intravenous delivery and the pathology is easier to assess

(Figure 5). However, even with this delivery route in our hands, occasionally the inner ear shows insufficient concentration of GdC in the perilymph and assessment of the disorder may be difficult.

Future development

1. ***Novel contrast agents:***

Novel highly sensitive, specific, and low-toxicity contrast agents for MRI and MDCT are in urgent need in the clinic. For MRI manganese-containing contrast agents would be most suitable as these can demonstrate the calcium metabolism that is inherent in disease processes in the inner ear (115) (116) (117) (118). Nanoparticle based GdC carrier can be are an effective MRI T1 contrast agent and have been used in high resolution MRI for tracing apoptosis and gene transcription in animal models of cerebral ischemia and brain tumours(119)(120). A novel type of super-paramagnetic iron oxide nanoparticles (SPIONs) that is water soluble, a characteristic that can be invaluable for medical applications has been designed (Fig. 7) (121, 122). It is constructed from iron oxide nanoparticle cores with a hierarchical coating consisting of a surface layer of Pluornic® F127 copolymer (PF127, approved by the Food and Drug Administration) that overlays a layer of oleic acid on the surface of the iron oxide nanoparticles (POA@SPIONs). POA@SPIONs is a promising T2 negative contrast agent that is detectable within the inner ear by MR imaging (123). Functionalization of POA@SPIONs can be performed and will make it targetable to inflammatory cytokines in the inner ear; however, the POA@SPIONs did not enter the inner ear efficiently after the transtympanic injection (106). Another novel highly hydrophilic anti-aggregative super-paramagnetic maghemite (γ-Fe_2O_3) nanoparticles (NPs) was developed using ceric ammonium nitrate (CAN)-mediated oxidation of starting magnetite (Fe_3O_4) NPs (CAN-γ-Fe_2O_3 NPs), which were highly stable aqueous suspensions/ferrofluids due to a unique ultrasound-mediated doping process of the Fe_3O_4 NP surface using lanthanide $Ce^{3/4+}$ cations (124). Zou et al. have also demonstrated that the novel CAN-γ-Fe_2O_3 NPs is a strong T_2 MRI contrast agent and penetrates both round and oval windows, which has potential applications in molecular imaging of the inner ear (125).

Figure 7. Super-paramagnetic iron oxide nanoparticles (*SPION) contrasted inner ear in rat. The SPION administered into the perilymph will extinguish the signal from the perilymph and only endolymphatic spaces are visible on MRI. Reprinted with permission of Europ J nanomed (122). Cochlea, vestibule and the semicircular canals are shown.*

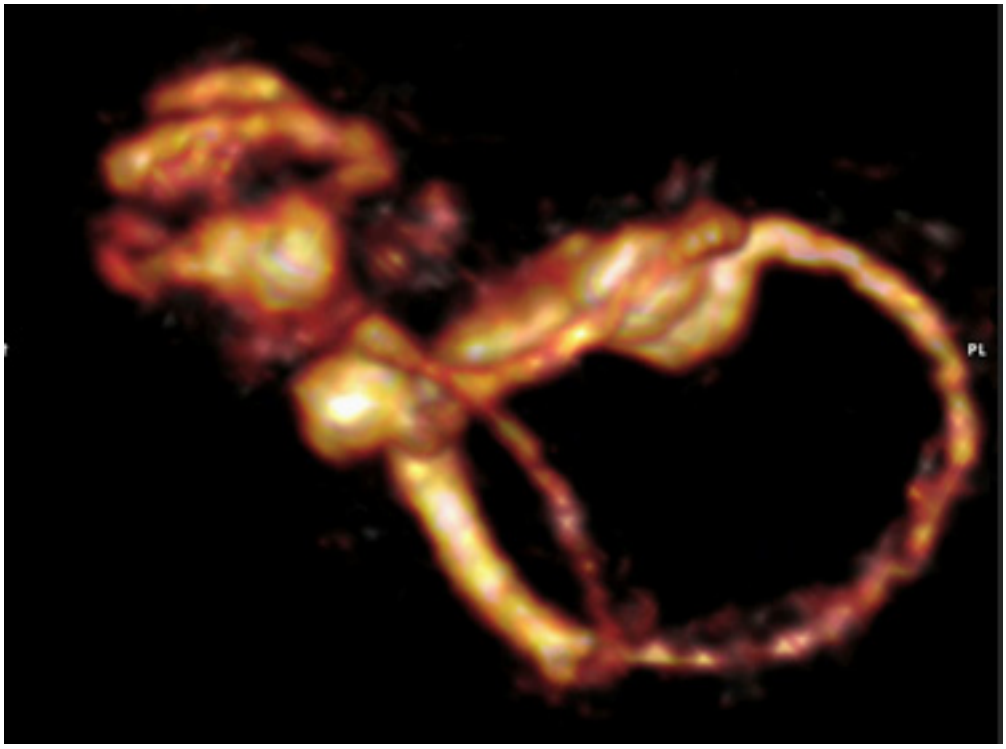

By developing a novel nanomaterial to be used as contrasting agent for example encapsulation of metals and metal clusters in fullerenes (endohedral metallofullerenes) opens additional vistas for inner ear imaging (126) (127) (128). The carbon cage has inherent advantages because of its high stability and characteristic resistance to any potential metabolic cage-opening process. This prevents the release of toxic metal ions from endohedral metallofullerenes into surrounding tissue, serum, and other biologic components (126). Water-soluble endohedral gadolinium-lutetium fullerene is generating considerable interest because of the possibility of using these novel nanomaterials as both MRI and MDCT imaging contrast agents. It is possible in the future medicine that specific molecular MRI and MDCT imaging can be performed after single injection of the targetable dual contrast agent.

2. Targeted contrast agents:

Contrast agents to enhance or darken fluid or tissue signals help to visualize regions of interest and efforts are now being made to create biological tags using these agents for molecular imaging at the level of cellular processes. Aimed to visualize liposome nanoparticles in the inner ear, GdC-encapsulated liposomes were developed and distribution of the nanoparticles in the cochlea was detected *in vivo* using MRI after either intracochlear injection or intratympanic injection (129-131). These studies open a window in specific visualization

of inner ear pathology using MRI. GdC-encapsulated liposomes pass through both the oval and round windows and was not toxic in in-vivo experiments. Potential molecular imaging in the inner ear using the novel CAN-γ-Fe_2O_3 NPs was also demonstrated in an animal study (132)The novel NPs are especially useful for molecular imaging of the inner ear to detect molecular changes in pathological conditions.

3. *Microtomgraphy (μCT)*

In CT the cochlear partition and soft tissue as membranes are not adequately visualized (10) (11). The gray levels in a CT slice image correspond to X-ray attenuation, which reflects the proportion of X-rays scattered or absorbed as they pass through each voxel, and is affected by the density and composition of the material being imaged. Non-destructive X-ray microtomography (μCT) has proven its utility in 3D assessment of mineralized and soft tissue morphology (133) (134). The cochlear partition and the basilar membrane could not be distinguished and reconstructed with μCT (134) Recently Poznyakovskiy et al. presented an algorithm for cochlear segmentation, which resulted in the reconstruction of scala tympani (135). μCT has been engaged in middle and inner ear imaging of animals and implicated to be a useful tool to trace distribution of drugs in the inner ear. However, it can only be used for *ex-vivo* imaging due to the extremely high dose of exposure and the close imaging distance which is only suitable for the head (136). The contrast enhanced μCT methodology is further developed for *ex-vivo* cochlear imaging (28). It can demonstrate the position of Reissner's membrane and basilar membrane if a contrast agent is used (136). Figure 8 demonstrates CI imaged with μCT. However, μCT produces extremely high radiation dose and in present form cannot be applied in humans.

Recently this technique has been advanced in animal experiments by revealing the inner ear compartment with simultaneous 9T MRI scanner and μCT (2). The combined MRI-μCT imaging techniques were complementary, and provided high-resolution dynamic and static visualization of the morphological features of the normal mouse inner ear structures.

Figure 8. Imaging of CI electrode with μCT, Left figure shows the base electrodes stimulating areas close to the round window, The right figure shows the first and second tip electerodes aimed to stinmulate apex of the cochlea. The bars indicate distance of 100 μm,

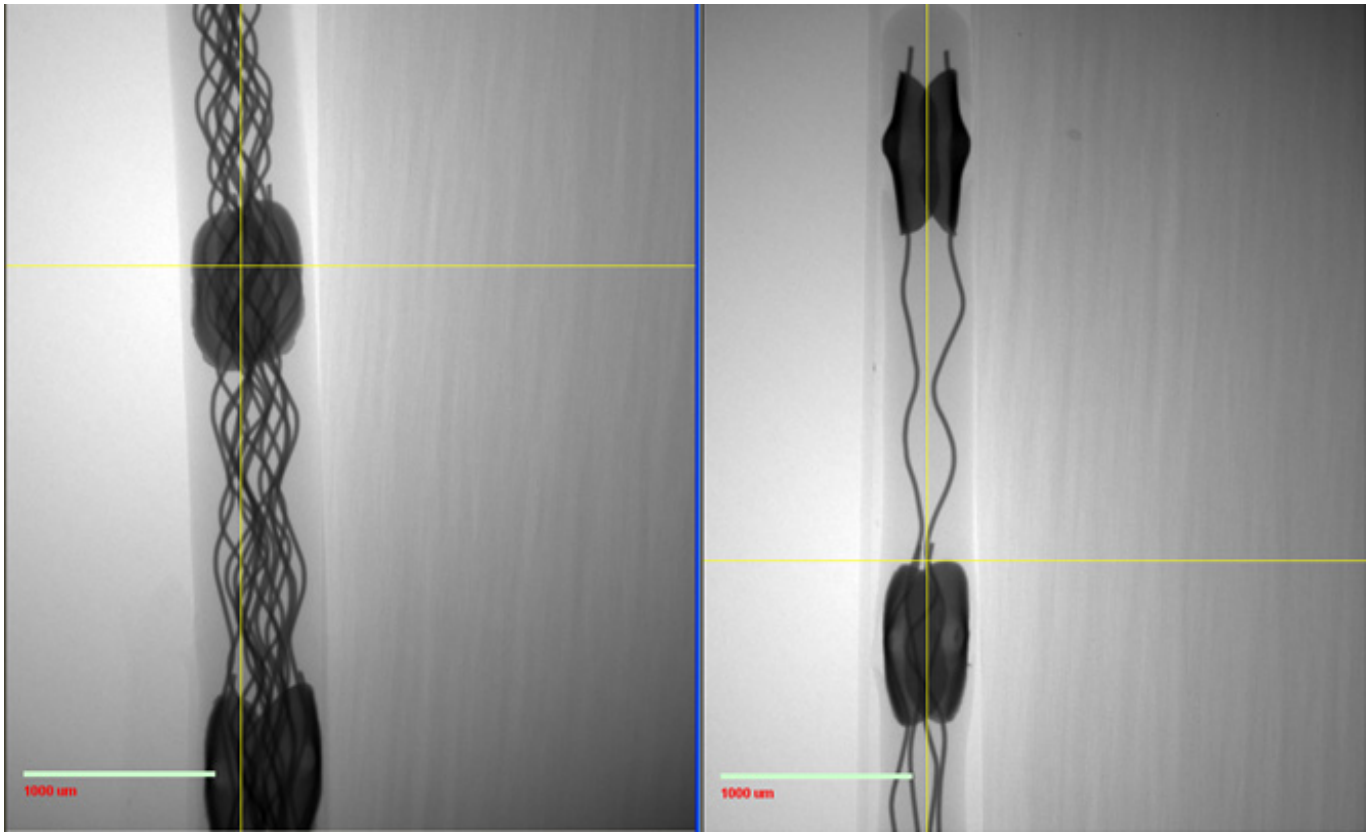

4. High-resolution coherent anti-Stokes Raman spectroscopy (CARS)

Raman spectroscopy is a powerful tool to generate a characteristic signature of specific tissues and operates by detecting energy with the molecular bond vibration of incident photons. The process results in non-elastically scattered light, also known as Raman scattering(137) Raman spectroscopy is capable of discerning molecular pathology of differential proliferative middle ear lesions and may provide an aid in assessment of the borders of the pathological process in order to improve surgical outcome of the middle ear diseases (138)(139)(140)(141)(7). CARS occurs when a target molecule is irradiated using two laser beams simultaneously at different frequencies, a pump beam and a Stokes beam. When the difference between the higher frequency (pump beam) and the lower frequency (Stokes beam) equals the vibrational frequency of the target bond of the molecule, a CARS signal is generated (139) (140) (141). Zou et al (7) has recently demonstrated the feasibility of using CARS microscopy to display the specific molecular morphology of cholesteatoma that has the potential to be integrated in a novel endoscope for cholesteatoma imaging in the clinic. There are reports on developing CARS endoscopes, although the system needs further improvement (142, 143).

Conclusions.

Temporal bone imaging should be sensitive enough to reveal functional disorders after trauma, inflammatory diseases, space occupying lesions such as cholesteatoma or vestibular schwannoma, changes in bone density such as otoscleosis, disruption of ossicular chain, various congenital anomalies, vascular malformations and position and insertion depth of cochlear implants. MDCT and CBCT have the benefit that they accurately describe the bony structures of the temporal bone. During CBCT imaging, the dose is applied to a very narrow section of the body with minimum exposure of the non-targeting area to radiation, and the total X-ray dose is lower compared with MDCT. In addition, CBCT's rapid data acquisition means that only a low dose of radiation is created during the imaging. MRI, especially at a field strength of 3T, is excellent in revealing changes of the soft tissues and fluid spaces in the temporal bone. The 3T MRI allows relatively accurate visualization of endolymphatic hydrops and even the membranous structures of the inner ear. Modern trends with targeted imaging of the inner ear may provide possibilities to visualize inner ear pathologies that can be assessed today only on histology. The recent imaging possibilities to explore inner ear fluid spaces are especially encouraging and contribute to clinical practice by defining Hydropic Ear Disease as a new entity.

References

1. DeMarcantonio M, Choo DI. Radiographic Evaluation of Children with Hearing Loss. Otolaryngol Clin North Am. 2015 Dec;48(6):913-32.
2. Counter SA, Damberg P, Aski SN, Nagy K, Berglin CE, Laurell G. Experimental Fusion of Contrast Enhanced High-Field Magnetic Resonance Imaging and High-Resolution Micro-Computed Tomography in Imaging the Mouse Inner Ear. Open Neuroimag J. 2015;9:7-12.
3. Pitris C, Saunders KT, Fujimoto JG, Brezinski ME. High-resolution imaging of the middle ear with optical coherence tomography: a feasibility study. Arch Otolaryngol Head Neck Surg. 2001 Jun;127(6):637-42.
4. Lin J, Staecker H, Jafri MS. Optical coherence tomography imaging of the inner ear: a feasibility study with implications for cochlear implantation. Ann Otol Rhinol Laryngol. 2008 May;117(5):341-6.
5. Cho NH, Jang JH, Jung W, Kim J. In vivo imaging of middle-ear and inner-ear microstructures of a mouse guided by SD-OCT combined with a surgical microscope. Opt Express. 2014 Apr 21;22(8):8985-95.
6. Zou J, Lahelma J, Koivisto J, Dhanasingh A, Jolly C, Aarnisalo A, et al. Imaging cochlear implantation with round window insertion in human temporal bones and cochlear morphological variation using high-resolution cone beam CT. Acta Otolaryngol. 2015 May;135(5):466-72.
7. Zou J, Isomäki, A, Hirvonen, T, Aarnisalo, A, Jero, J, Pyykkö I. Label-free visualization of cholesteatoma in the mastoid and tympanic membrane using CARS microscopy. J Otol. 2016;11 (3):127-33.
8. Zou J, Pyykko, I., Hyttinen J,. Inner ear barriers to nanomedicine-augmented drug delivery and imaging. . Journal of Otology. 2016;11(4):165-77.
9. Giesemann A, Hofmann E. Some Remarks on Imaging of the Inner Ear: Options and Limitations. Clin Neuroradiol. 2015 Oct;25 Suppl 2:197-203.
10. Shibata T, Nagano T. Applying very high resolution microfocus X-ray CT and 3-D reconstruction to the human auditory apparatus. Nat Med. 1996 Aug;2(8):933-5.
11. Vogel U. New approach for 3D imaging and geometry modeling of the human inner ear. ORL J Otorhinolaryngol Relat Spec. 1999 Sep-Oct;61(5):259-67.
12. Maillot O, Attye A, Boyer E, Heck O, Kastler A, Grand S, et al. Post traumatic deafness: a pictorial review of CT and MRI findings. Insights Imaging. 2016 Jun;7(3):341-50.
13. Lane JI, Lindell EP, Witte RJ, DeLone DR, Driscoll CL. Middle and inner ear: improved depiction with multiplanar reconstruction of volumetric CT data. Radiographics. 2006 Jan-Feb;26(1):115-24.
14. Fatterpekar GM, Doshi AH, Dugar M, Delman BN, Naidich TP, Som PM. Role of 3D CT in the evaluation of the temporal bone. Radiographics. 2006 Oct;26 Suppl 1:S117-32.
15. Gnagi SH, Baker TR, Pollei TR, Barrs DM. Analysis of Intraoperative Radiographic Electrode Placement During Cochlear Implantation. Otol Neurotol. 2015 Jul;36(6):1045-7.
16. Carlson ML, Leng S, Diehn FE, Witte RJ, Krecke KN, Grimes J, et al. Cochlear Implant Electrode Localization Using an Ultra-High Resolution Scan Mode on Conventional 64-Slice and New Generation 192-Slice Multi-Detector Computed Tomography. Otol Neurotol. 2017 Aug;38(7):978-84.
17. Tavassolie TS, Penninger RT, Zuniga MG, Minor LB, Carey JP. Multislice computed tomography in the diagnosis of superior canal dehiscence: how much error, and how to minimize it? Otol Neurotol. 2012 Feb;33(2):215-22.
18. Bremke M, Luers JC, Anagiotos A, Gostian AO, Dorn F, Kabbasch C, et al. Comparison of digital volume tomography and high-resolution computed tomography in detecting superior semicircular canal dehiscence--a temporal bone study. Acta Otolaryngol. 2015 Sep;135(9):901-6.
19. Brantberg K, Greitz D, Pansell T. Subarcuate venous malformation causing audio-vestibular symptoms similar to those in superior canal dehiscence syndrome. Otol Neurotol. 2004 Nov;25(6):993-7.
20. Institute NC. Radiation Risks and Pediatric Computed Tomography (CT): A Guide for Health Care Providers. https://wwwcancergov/about-cancer/causes-prevention/risk/radiation/pediatric-ct-scans. 2012.
21. Brenner D, Elliston C, Hall E, Berdon W. Estimated risks of radiation-induced fatal cancer from pediatric CT. AJR Am J Roentgenol. 2001 Feb;176(2):289-96.
22. Pearce MS, Salotti JA, Little MP, McHugh K, Lee C, Kim KP, et al. Radiation exposure from CT scans in childhood and subsequent risk of leukaemia and brain tumours: a retrospective cohort study. Lancet. 2012 Aug 4;380(9840):499-505.

23. Little MP, Hoel DG, Molitor J, Boice JD, Wakeford R, Muirhead CR. New models for evaluation of radiation-induced lifetime cancer risk and its uncertainty employed in the UNSCEAR 2006 report. Radiat Res. 2008 Jun;169(6):660-76.
24. DJ B, Elliston CD, Hall EJ, WE. B. Estimated Risks of RadiationInduced Fatal Cancer from Pediatric CT. AJR. 2001;176(289-296).
25. Nauer CB, Zubler C, Weisstanner C, Stieger C, Senn P, Arnold A. Radiation dose optimization in pediatric temporal bone computed tomography: influence of tube tension on image contrast and image quality. Neuroradiology. 2012 Mar;54(3):247-54.
26. Weisstanner C, Mantokoudis G, Huth M, Verma RK, Nauer C, Senn P, et al. Radiation dose reduction in postoperative computed position control of cochlear implant electrodes in lambs - An experimental study. Int J Pediatr Otorhinolaryngol. 2015 Dec;79(12):2348-54.
27. Erovic BM, Chan HH, Daly MJ, Pothier DD, Yu E, Coulson C, et al. Intraoperative cone-beam computed tomography and multi-slice computed tomography in temporal bone imaging for surgical treatment. Otolaryngol Head Neck Surg. 2014 Jan;150(1):107-14.
28. Zou J, Hannula M, Lehto K, Feng H, Lahelma J, Aula AS, et al. X-ray microtomographic confirmation of the reliability of CBCT in identifying the scalar location of cochlear implant electrode after round window insertion. Hear Res. 2015 Aug;326:59-65.
29. Kakinuma R, Moriyama N, Muramatsu Y, Gomi S, Suzuki M, Nagasawa H, et al. Ultra-High-Resolution Computed Tomography of the Lung: Image Quality of a Prototype Scanner. PLoS One. 2015;10(9):e0137165.
30. Peltonen LI, Aarnisalo AA, Kortesniemi MK, Suomalainen A, Jero J, Robinson S. Limited cone-beam computed tomography imaging of the middle ear: a comparison with multislice helical computed tomography. Acta Radiol. 2007 Mar;48(2):207-12.
31. Kurt H, Orhan K, Aksoy S, Kursun S, Akbulut N, Bilecenoglu B. Evaluation of the superior semicircular canal morphology using cone beam computed tomography: a possible correlation for temporomandibular joint symptoms. Oral Surg Oral Med Oral Pathol Oral Radiol. 2014 Mar;117(3):e280-8.
32. Rafferty MA, Siewerdsen JH, Chan Y, Daly MJ, Moseley DJ, Jaffray DA, et al. Intraoperative cone-beam CT for guidance of temporal bone surgery. Otolaryngol Head Neck Surg. 2006 May;134(5):801-8.
33. Mlynski R, Nguyen TD, Plontke SK, Kosling S. Presentation of floating mass transducer and Vibroplasty couplers on CT and cone beam CT. Eur Arch Otorhinolaryngol. 2014 Apr;271(4):665-72.
34. Razafindranaly V, Truy E, Pialat JB, Martinon A, Bourhis M, Boublay N, et al. Cone Beam CT Versus Multislice CT: Radiologic Diagnostic Agreement in the Postoperative Assessment of Cochlear Implantation. Otol Neurotol. 2016 Oct;37(9):1246-54.
35. Zhu L, Xie Y, Wang J, Xing L. Scatter correction for cone-beam CT in radiation therapy. Med Phys. 2009 Jun;36(6):2258-68.
36. Mail N, Moseley DJ, Siewerdsen JH, Jaffray DA. An empirical method for lag correction in cone-beam CT. Med Phys. 2008 Nov;35(11):5187-96.
37. Meilinger M, Schmidgunst C, Schutz O, Lang EW. Metal artifact reduction in cone beam computed tomography using forward projected reconstruction information. Z Med Phys. 2011 Sep;21(3):174-82.
38. Guldner C, Wiegand S, Weiss R, Bien S, Sesterhenn A, Teymoortash A, et al. Artifacts of the electrode in cochlea implantation and limits in analysis of deep insertion in cone beam tomography (CBT). Eur Arch Otorhinolaryngol. 2012 Mar;269(3):767-72.
39. Gupta R, Bartling SH, Basu SK, Ross WR, Becker H, Pfoh A, et al. Experimental flat-panel high-spatial-resolution volume CT of the temporal bone. AJNR Am J Neuroradiol. 2004 Sep;25(8):1417-24.
40. Diogo I, Franke N, Steinbach-Hundt S, Mandapathil M, Weiss R, Werner JA, et al. Differences of radiological artefacts in cochlear implantation in temporal bone and complete head. Cochlear Implants Int. 2014 Mar;15(2):112-7.
41. Pearl MS, Roy A, Limb CJ. High-resolution secondary reconstructions with the use of flat panel CT in the clinical assessment of patients with cochlear implants. AJNR Am J Neuroradiol. 2014 Jun;35(6):1202-8.
42. Ruivo J, Mermuys K, Bacher K, Kuhweide R, Offeciers E, Casselman JW. Cone beam computed tomography, a low-dose imaging technique in the postoperative assessment of cochlear implantation. Otol Neurotol. 2009 Apr;30(3):299-303.
43. Verbist BM, Frijns JH, Geleijns J, van Buchem MA. Multisection CT as a valuable tool in the postoperative assessment of cochlear implant patients. AJNR Am J Neuroradiol. 2005 Feb;26(2):424-9.

44. Trieger A, Schulze A, Schneider M, Zahnert T, Murbe D. In vivo measurements of the insertion depth of cochlear implant arrays using flat-panel volume computed tomography. Otol Neurotol. 2011 Jan;32(1):152-7.
45. Struffert T, Hertel V, Kyriakou Y, Krause J, Engelhorn T, Schick B, et al. Imaging of cochlear implant electrode array with flat-detector CT and conventional multislice CT: comparison of image quality and radiation dose. Acta Otolaryngol. 2010 Apr;130(4):443-52.
46. Zou J, Koivisto J, Lahelma J, Aarnisalo A, Wolff J, Pyykko I. Imaging Optimization of Temporal Bones With Cochlear Implant Using a High-resolution Cone Beam CT and the Corresponding Effective Dose. Ann Otol Rhinol Laryngol. 2015 Jun;124(6):466-73.
47. Zou J. Lähelmä J, Aarnisalo A, Pyykko I, . Clinically relevant human temporal bone measurements using novel high-resolution cone-beam CT. Journal of otology. 2017;12(1):9-17.
48. Theunisse HJ, Joemai RM, Maal TJ, Geleijns J, Mylanus EA, Verbist BM. Cone-beam CT versus multi-slice CT systems for postoperative imaging of cochlear implantation--a phantom study on image quality and radiation exposure using human temporal bones. Otol Neurotol. 2015 Apr;36(4):592-9.
49. Yamane H, Iguchi H, Konishi K, Sakamaoto H, Wada T, Fujioka T, et al. Three-dimensional cone beam computed tomography imaging of the membranous labyrinth in patients with Meniere's disease. Acta Otolaryngol. 2014 Oct;134(10):1016-21.
50. Koivisto J, Kiljunen T, Wolff J, Kortesniemi M. Assessment of effective radiation dose of an extremity CBCT, MSCT and conventional X ray for knee area using MOSFET dosemeters. Radiat Prot Dosimetry. 2013 Dec;157(4):515-24.
51. Kim DS, Rashsuren O, Kim EK. Conversion coefficients for the estimation of effective dose in cone-beam CT. Imaging Sci Dent. 2014 Mar;44(1):21-9.
52. Daly MJ, Siewerdsen JH, Moseley DJ, Jaffray DA, Irish JC. Intraoperative cone-beam CT for guidance of head and neck surgery: Assessment of dose and image quality using a C-arm prototype. Med Phys. 2006 Oct;33(10):3767-80.
53. Naganawa S, Nakane T, Kawai H, Taoka T, Suzuki K, Iwano S, et al. Visualization of Middle Ear Ossicles in Elder Subjects with Ultra-short Echo Time MR Imaging. Magn Reson Med Sci. 2017 Apr 10;16(2):93-7.
54. Naganawa S, Koshikawa T, Nakamura T, Fukatsu H, Ishigaki T, Aoki I. High-resolution T1-weighted 3D real IR imaging of the temporal bone using triple-dose contrast material. Eur Radiol. 2003 Dec;13(12):2650-8.
55. Naganawa S, Satake H, Kawamura M, Fukatsu H, Sone M, Nakashima T. Separate visualization of endolymphatic space, perilymphatic space and bone by a single pulse sequence; 3D-inversion recovery imaging utilizing real reconstruction after intratympanic Gd-DTPA administration at 3 Tesla. Eur Radiol. 2008 May;18(5):920-4.
56. Naganawa S, Kawai H, Sone M, Nakashima T. Increased sensitivity to low concentration gadolinium contrast by optimized heavily T2-weighted 3D-FLAIR to visualize endolymphatic space. Magn Reson Med Sci. 2010;9(2):73-80.
57. Naganawa S, Kawai H, Ikeda M, Sone M, Nakashima T. Imaging of endolymphatic hydrops in 10 minutes: a new strategy to reduce scan time to one third. Magn Reson Med Sci. 2015;14(1):77-83.
58. Naganawa S, Nakashima T. Visualization of endolymphatic hydrops with MR imaging in patients with Meniere's disease and related pathologies: current status of its methods and clinical significance. Jpn J Radiol. 2014 Apr;32(4):191-204.
59. Nakashima T, Pyykko I, Arroll MA, Casselbrant ML, Foster CA, Manzoor NF, et al. Meniere's disease. Nat Rev Dis Primers. 2016;2:16028.
60. Counter SA, Bjelke B, Klason T, Chen Z, Borg E. Magnetic resonance imaging of the cochlea, spiral ganglia and eighth nerve of the guinea pig. Neuroreport. 1999 Feb 25;10(3):473-9.
61. Zou J, Pyykko I, Bretlau P, Klason T, Bjelke B. In vivo visualization of endolymphatic hydrops in guinea pigs: magnetic resonance imaging evaluation at 4.7 tesla. Ann Otol Rhinol Laryngol. 2003 Dec;112(12):1059-65.
62. Zou J P, I, Bjelke B, Bretlau P, Tayamaga T. . Endolympahtic hydrops is caused by increased porosity of stria vascularis? . Barany Society Meeting; Uppsala, Sweden 2000. 2000.
63. Niyazov DM, Andrews JC, Strelioff D, Sinha S, Lufkin R. Diagnosis of endolymphatic hydrops in vivo with magnetic resonance imaging. Otol Neurotol. 2001 Nov;22(6):813-7.
64. Zou J, Pyykko I, Bjelke B, Dastidar P, Toppila E. Communication between the perilymphatic scalae and spiral ligament visualized by in vivo MRI. Audiol Neurootol. 2005 May-Jun;10(3):145-52.
65. Nakashima T, Naganawa S, Sugiura M, Teranishi M, Sone M, Hayashi H, et al. Visualization of endolymphatic hydrops in patients with Meniere's disease. Laryngoscope. 2007 Mar;117(3):415-20.

66. Pyykko I, Zou J, Poe D, Nakashima T, Naganawa S. Magnetic resonance imaging of the inner ear in Meniere's disease. Otolaryngol Clin North Am. 2010 Oct;43(5):1059-80.
67. Gurkov R, Flatz W, Louza J, Strupp M, Krause E. In vivo visualization of endolyphatic hydrops in patients with Meniere's disease: correlation with audiovestibular function. Eur Arch Otorhinolaryngol. 2011 Dec;268(12):1743-8.
68. Naganawa S, Yamazaki M, Kawai H, Bokura K, Iida T, Sone M, et al. MR imaging of Meniere's disease after combined intratympanic and intravenous injection of gadolinium using HYDROPS2. Magn Reson Med Sci. 2014;13(2):133-7.
69. Nakashima T, Sone M, Teranishi M, Yoshida T, Terasaki H, Kondo M, et al. A perspective from magnetic resonance imaging findings of the inner ear: Relationships among cerebrospinal, ocular and inner ear fluids. Auris Nasus Larynx. 2012 Aug;39(4):345-55.
70. Nakashima T, Naganawa S, Pyykko I, Gibson WP, Sone M, Nakata S, et al. Grading of endolymphatic hydrops using magnetic resonance imaging. Acta Otolaryngol Suppl. 2009 Feb(560):5-8.
71. Pyykko I, Nakashima T, Yoshida T, Zou J, Naganawa S. Meniere's disease: a reappraisal supported by a variable latency of symptoms and the MRI visualisation of endolymphatic hydrops. BMJ Open. 2013;3(2).
72. Gurkov R, Flatz W, Louza J, Strupp M, Ertl-Wagner B, Krause E. In vivo visualized endolymphatic hydrops and inner ear functions in patients with electrocochleographically confirmed Meniere's disease. Otol Neurotol. 2012 Aug;33(6):1040-5.
73. Liu F, Huang W, Wang Z, Chen Q, Liu X, Li S, et al. Noninvasive evaluation of endolymphatic space in healthy volunteers using magnetic resonance imaging. Acta Otolaryngol. 2011 Mar;131(3):247-57.
74. Counter SA, Bjelke B, Borg E, Klason T, Chen Z, Duan ML. Magnetic resonance imaging of the membranous labyrinth during in vivo gadolinium (Gd-DTPA-BMA) uptake in the normal and lesioned cochlea. Neuroreport. 2000 Dec 18;11(18):3979-83.
75. Zou J, Pyykko I, Counter SA, Klason T, Bretlau P, Bjelke B. In vivo observation of dynamic perilymph formation using 4.7 T MRI with gadolinium as a tracer. Acta Otolaryngol. 2003 Oct;123(8):910-5.
76. Zou J, Zhang W, Poe D, Zhang Y, Ramadan UA, Pyykko I. Differential passage of gadolinium through the mouse inner ear barriers evaluated with 4.7T MRI. Hear Res. 2010 Jan;259(1-2):36-43.
77. Zou J, Yoshida T, Ramadan UA, Pyykko I. Dynamic enhancement of the rat inner ear after ultra-small-volume administration of Gd-DOTA to the medial wall of the middle ear cavity. ORL J Otorhinolaryngol Relat Spec. 2011;73(5):275-81.
78. Zou J, Pyykko I. Enhanced oval window and blocked round window passages for middle-inner ear transportation of gadolinium in guinea pigs with a perforated round window membrane. Eur Arch Otorhinolaryngol. 2015 Feb;272(2):303-9.
79. Kaasinen S, Pyykko I, Ishizaki H, Aalto H. Intratympanic gentamicin in Meniere's disease. Acta Otolaryngol. 1998 Jun;118(3):294-8.
80. Eklund S, Pyykko I, Aalto H, Ishizaki H, Vasama JP. Effect of intratympanic gentamicin on hearing and tinnitus in Meniere's disease. Am J Otol. 1999 May;20(3):350-6.
81. Louza JP, Flatz W, Krause E, Gurkov R. Short-term audiologic effect of intratympanic gadolinium contrast agent application in patients with Meniere's disease. Am J Otolaryngol. 2012 Sep-Oct;33(5):533-7.
82. Louza J, Krause E, Gurkov R. Audiologic evaluation of Meniere's disease patients one day and one week after intratympanic application of gadolinium contrast agent: our experience in sixty-five patients. Clin Otolaryngol. 2013 Jun;38(3):262-6.
83. Louza J, Krause E, Gurkov R. Hearing function after intratympanic application of gadolinium-based contrast agent: A long-term evaluation. Laryngoscope. 2015 Oct;125(10):2366-70.
84. Yoshioka M, Naganawa S, Sone M, Nakata S, Teranishi M, Nakashima T. Individual differences in the permeability of the round window: evaluating the movement of intratympanic gadolinium into the inner ear. Otol Neurotol. 2009 Aug;30(5):645-8.
85. Naganawa S, Yamazaki M, Kawai H, Bokura K, Sone M, Nakashima T. Imaging of Meniere's disease after intravenous administration of single-dose gadodiamide: utility of subtraction images with different inversion time. Magn Reson Med Sci. 2012;11(3):213-9.
86. Wu Q, Dai C, Zhao M, Sha Y. The correlation between symptoms of definite Meniere's disease and endolymphatic hydrops visualized by magnetic resonance imaging. Laryngoscope. 2016 Apr;126(4):974-9.

87. Yamazaki M, Naganawa S, Tagaya M, Kawai H, Ikeda M, Sone M, et al. Comparison of contrast effect on the cochlear perilymph after intratympanic and intravenous gadolinium injection. AJNR Am J Neuroradiol. 2012 Apr;33(4):773-8.
88. Naganawa S, Yamazaki M, Kawai H, Bokura K, Sone M, Nakashima T. Visualization of endolymphatic hydrops in Meniere's disease with single-dose intravenous gadolinium-based contrast media using heavily T(2)-weighted 3D-FLAIR. Magn Reson Med Sci. 2010;9(4):237-42.
89. Attye A, Dumas G, Tropres I, Roustit M, Karkas A, Banciu E, et al. Recurrent peripheral vestibulopathy: Is MRI useful for the diagnosis of endolymphatic hydrops in clinical practice? Eur Radiol. 2015 Oct;25(10):3043-9.
90. Pakdaman MN, Ishiyama G, Ishiyama A, Peng KA, Kim HJ, Pope WB, et al. Blood-Labyrinth Barrier Permeability in Meniere Disease and Idiopathic Sudden Sensorineural Hearing Loss: Findings on Delayed Postcontrast 3D-FLAIR MRI. AJNR Am J Neuroradiol. 2016 Jun 2.
91. Tanigawa T, Tamaki T, Yamamuro O, Tanaka H, Nonoyama H, Shiga A, et al. Visualization of endolymphatic hydrops after administration of a standard dose of an intravenous gadolinium-based contrast agent. Acta Otolaryngol. 2011 Jun;131(6):596-601.
92. Mukaida T, Sone M, Yoshida T, Kato K, Teranishi M, Naganawa S, et al. Magnetic Resonance Imaging Evaluation of Endolymphatic Hydrops in Cases With Otosclerosis. Otol Neurotol. 2015 Aug;36(7):1146-50.
93. Gurkov R, Berman A, Dietrich O, Flatz W, Jerin C, Krause E, et al. MR volumetric assessment of endolymphatic hydrops. Eur Radiol. 2015 Feb;25(2):585-95.
94. Naganawa S. The Technical and Clinical Features of 3D-FLAIR in Neuroimaging. Magn Reson Med Sci. 2015;14(2):93-106.
95. Naganawa S, Ohashi T, Kanou M, Kuno K, Sone M, Ikeda M. Volume Quantification of Endolymph after Intravenous Administration of a Single Dose of Gadolinium Contrast Agent: Comparison of 18- versus 8-minute Imaging Protocols. Magn Reson Med Sci. 2015;14(4):257-62.
96. Naganawa S, Kawai H, Taoka T, Sone M. Improved 3D-real Inversion Recovery: A Robust Imaging Technique for Endolymphatic Hydrops after Intravenous Administration of Gadolinium. Magn Reson Med Sci. 2018 Mar 7.
97. Fiorino F, Pizzini FB, Beltramello A, Mattellini B, Barbieri F. Reliability of magnetic resonance imaging performed after intratympanic administration of gadolinium in the identification of endolymphatic hydrops in patients with Meniere's disease. Otol Neurotol. 2011 Apr;32(3):472-7.
98. Shi H, Li Y, Yin S, Zou J. The predominant vestibular uptake of gadolinium through the oval window pathway is compromised by endolymphatic hydrops in Meniere's disease. Otol Neurotol. 2014 Feb;35(2):315-22.
99. Fiorino F, Pizzini FB, Beltramello A, Barbieri F. Progression of endolymphatic hydrops in Meniere's disease as evaluated by magnetic resonance imaging. Otol Neurotol. 2011 Sep;32(7):1152-7.
100. Gurkov R, Flatz W, Ertl-Wagner B, Krause E. Endolymphatic hydrops in the horizontal semicircular canal: a morphologic correlate for canal paresis in Meniere's disease. Laryngoscope. 2013 Feb;123(2):503-6.
101. Jerin C, Krause E, Ertl-Wagner B, Gurkov R. Longitudinal assessment of endolymphatic hydrops with contrast-enhanced magnetic resonance imaging of the labyrinth. Otol Neurotol. 2014 Jun;35(5):880-3.
102. Suga K, Kato M, Yoshida T, Nishio N, Nakada T, Sugiura S, et al. Changes in endolymphatic hydrops in patients with Meniere's disease treated conservatively for more than 1 year. Acta Otolaryngol. 2015 Sep;135(9):866-70.
103. Maxwell R, Jerin C, Gurkov R. Utilisation of multi-frequency VEMPs improves diagnostic accuracy for Meniere's disease. Eur Arch Otorhinolaryngol. 2017 Jan;274(1):85-93.
104. Naganawa S, Yamazaki M, Kawai H, Bokura K, Sone M, Nakashima T. Imaging of Meniere's disease by subtraction of MR cisternography from positive perilymph image. Magn Reson Med Sci. 2012;11(4):303-9.
105. Huang CH, Young YH. Bilateral Meniere's disease assessed by an inner ear test battery. Acta Otolaryngol. 2015 Mar;135(3):233-8.
106. Friberg U, Stahle J, Svedberg A. The natural course of Meniere's disease. Acta Otolaryngol Suppl. 1984;406:72-7.
107. Thomas K, Harrison MS. Long-term follow up of 610 cases of Meniere's disease. Proc R Soc Med. 1971 Aug;64(8):853-7.
108. House JW, Doherty JK, Fisher LM, Derebery MJ, Berliner KI. Meniere's disease: prevalence of contralateral ear involvement. Otol Neurotol. 2006 Apr;27(3):355-61.
109. Huppert D, Strupp M, Brandt T. Long-term course of Meniere's disease revisited. Acta Otolaryngol. 2010 Jun;130(6):644-51.

110. Gurkov R, Pyyko I, Zou J, Kentala E. What is Meniere's disease? A contemporary re-evaluation of endolymphatic hydrops. J Neurol. 2016 Apr;263 Suppl 1:S71-81.
111. Gurkov R, Flatz W, Louza J, Strupp M, Ertl-Wagner B, Krause E. Herniation of the membranous labyrinth into the horizontal semicircular canal is correlated with impaired caloric response in Meniere's disease. Otol Neurotol. 2012 Oct;33(8):1375-9.
112. Zellhuber S, Mahringer A, Rambold HA. Relation of video-head-impulse test and caloric irrigation: a study on the recovery in unilateral vestibular neuritis. Eur Arch Otorhinolaryngol. 2014 Sep;271(9):2375-83.
113. Mahringer A, Rambold HA. Caloric test and video-head-impulse: a study of vertigo/dizziness patients in a community hospital. Eur Arch Otorhinolaryngol. 2014 Mar;271(3):463-72.
114. Jerin C, Maxwell R, Gurkov R. High-Frequency Horizontal Semicircular Canal Function in Certain Meniere's Disease. Ear Hear. 2018 May 14.
115. Zou J, Pyykko I. Calcium Metabolism Profile in Rat Inner Ear Indicated by MRI After Tympanic Medial Wall Administration of Manganese Chloride. Ann Otol Rhinol Laryngol. 2016 Jan;125(1):53-62.
116. Zou J, Zhang Y, Yin S, Wu H, Pyykko I. Mitochondrial dysfunction disrupts trafficking of Kir4.1 in spiral ganglion satellite cells. J Neurosci Res. 2009 Jan;87(1):141-9.
117. Zou J, Zhang Y, Zhang W, Poe D, Zhai S, Yang S, et al. Mitochondria toxin-induced acute cochlear cell death indicates cellular activity-correlated energy consumption. Eur Arch Otorhinolaryngol. 2013 Sep;270(9):2403-15.
118. Groschel M, Hubert N, Muller S, Ernst A, Basta D. Age-dependent changes of calcium related activity in the central auditory pathway. Exp Gerontol. 2014 Oct;58:235-43.
119. Fatouros PP, Corwin FD, Chen ZJ, Broaddus WC, Tatum JL, Kettenmann B, et al. In vitro and in vivo imaging studies of a new endohedral metallofullerene nanoparticle. Radiology. 2006 Sep;240(3):756-64.
120. Fillmore HL, Shultz MD, Henderson SC, Cooper P, Broaddus WC, Chen ZJ, et al. Conjugation of functionalized gadolinium metallofullerenes with IL-13 peptides for targeting and imaging glial tumors. Nanomedicine (Lond). 2011 Apr;6(3):449-58.
121. Poe D ZJ, Zhang W, Qin J, Abo Ramadan U, Fornara A, Muhammed M, Pyykkö I. . MRI of the Cochlea with Superparamagnetic Iron Oxide Nanoparticles Compared to Gadolinium Chelate Contrast Agents in a Rat Model. . Europ J nanomed 2009;2:29-36. .
122. Fornara A, Johansson P, Petersson K, Gustafsson S, Qin J, Olsson E, et al. Tailored magnetic nanoparticles for direct and sensitive detection of biomolecules in biological samples. Nano Lett. 2008 Oct;8(10):3423-8.
123. Zou J, Zhang W, Poe D, Qin J, Fornara A, Zhang Y, et al. MRI manifestation of novel superparamagnetic iron oxide nanoparticles in the rat inner ear. Nanomedicine (Lond). 2010 Jul;5(5):739-54.
124. Haviv AH, Greneche JM, Lellouche JP. Aggregation control of hydrophilic maghemite (gamma-Fe2O3) nanoparticles by surface doping using cerium atoms. J Am Chem Soc. 2010 Sep 15;132(36):12519-21.
125. Zou J, Ostrovsky S, Israel LL, Feng H, Kettunen MI, Lellouche JM, et al. Efficient penetration of ceric ammonium nitrate oxidant-stabilized gamma-maghemite nanoparticles through the oval and round windows into the rat inner ear as demonstrated by MRI. J Biomed Mater Res B Appl Biomater. 2017 Oct;105(7):1883-91.
126. Zhen M, Zheng J, Wang Y, Shu C, Gao F, Zou J, et al. Multifunctional nanoprobe for MRI/optical dual-modality imaging and radical scavenging. Chemistry. 2013 Oct 18;19(43):14675-81.
127. Pyykko I, Zou J, Schrott-Fischer A, Glueckert R, Kinnunen P. An Overview of Nanoparticle Based Delivery for Treatment of Inner Ear Disorders. Methods Mol Biol. 2016;1427:363-415.
128. Zou J, Pyykkö I, Yoshida T, Gürkov R, Shi H, Li Y, Zheng G, Peng R, Zheng H, Yin Y, Hyttinen J, Nakashima T, Naganawa S. . A milestone research in Meniere's disease by visualizing endolymphatic hydrops using gadolinium-enhanced inner ear MRI and the challenges in clinical application. . Austin J Radiol 2015;2(6):1-7.
129. Zou J, Sood R, Ranjan S, Poe D, Ramadan UA, Kinnunen PK, et al. Manufacturing and in vivo inner ear visualization of MRI traceable liposome nanoparticles encapsulating gadolinium. J Nanobiotechnology. 2010;8:32.
130. Zou J, Sood R, Ranjan S, Poe D, Ramadan UA, Pyykko I, et al. Size-dependent passage of liposome nanocarriers with preserved posttransport integrity across the middle-inner ear barriers in rats. Otol Neurotol. 2012 Jun;33(4):666-73.
131. Zou J, Sood R, Zhang Y, Kinnunen PK, Pyykko I. Pathway and morphological transformation of liposome nanocarriers after release from a novel sustained inner-ear delivery system. Nanomedicine (Lond). 2014 Jul;9(14):2143-55.
132. Zou J PB, Ostrovsky S, Li B, Li C, Kettunen MI, Lellouche JM, Pyykkö I. Biological effect tetra-branched anti-TNF-peptide and coating ratio-dependent penetration of the peptide-conjugated Cerium3/4+ Cation-stabilized

gamma-maghemite nanoparticles into rat inner ear after transtympanic injection visualized by MRI. Journal of Materials Science & Nanotechnology 2017;In Press.
133. Bellos C, Rigas G, Spiridon IF, Bibas A, Iliopoulou D, Bohnke F, et al. Reconstruction of cochlea based on micro-CT and histological images of the human inner ear. Biomed Res Int. 2014;2014:485783.
134. Poznyakovskiy AA, Zahnert T, Kalaidzidis Y, Schmidt R, Fischer B, Baumgart J, et al. The creation of geometric three-dimensional models of the inner ear based on micro computer tomography data. Hear Res. 2008 Sep;243(1-2):95-104.
135. Poznyakovskiy AA, Mainka A, Platzek I, Murbe D. A Fast Semiautomatic Algorithm for Centerline-Based Vocal Tract Segmentation. Biomed Res Int. 2015;2015:906356.
136. Zou J, Hannula M, Misra S, Feng H, Labrador RH, Aula AS, et al. Micro CT visualization of silver nanoparticles in the middle and inner ear of rat and transportation pathway after transtympanic injection. J Nanobiotechnology. 2015;13:5.
137. Wachsmann-Hogiu S, Weeks T, Huser T. Chemical analysis in vivo and in vitro by Raman spectroscopy--from single cells to humans. Curr Opin Biotechnol. 2009 Feb;20(1):63-73.
138. Pandey R, Paidi SK, Kang JW, Spegazzini N, Dasari RR, Valdez TA, et al. Discerning the differential molecular pathology of proliferative middle ear lesions using Raman spectroscopy. Sci Rep. 2015;5:13305.
139. Rodriguez LG, Lockett SJ, Holtom GR. Coherent anti-stokes Raman scattering microscopy: a biological review. Cytometry A. 2006 Aug 1;69(8):779-91.
140. Folick A, Min W, Wang MC. Label-free imaging of lipid dynamics using Coherent Anti-stokes Raman Scattering (CARS) and Stimulated Raman Scattering (SRS) microscopy. Curr Opin Genet Dev. 2011 Oct;21(5):585-90.
141. Pezacki JP, Blake JA, Danielson DC, Kennedy DC, Lyn RK, Singaravelu R. Chemical contrast for imaging living systems: molecular vibrations drive CARS microscopy. Nat Chem Biol. 2011 Mar;7(3):137-45.
142. Brustlein S, Berto P, Hostein R, Ferrand P, Billaudeau C, Marguet D, et al. Double-clad hollow core photonic crystal fiber for coherent Raman endoscope. Opt Express. 2011 Jun 20;19(13):12562-8.
143. Wang Z, Gao L, Luo P, Yang Y, Hammoudi AA, Wong KK, et al. Coherent anti-Stokes Raman scattering microscopy imaging with suppression of four-wave mixing in optical fibers. Opt Express. 2011 Apr 25;19(9):7960-70.